Integrated study of first principles calculations and experimental measurements for Li-ionic conductivity in Al-doped solid-state LiGe$_2$(PO$_4$)$_3$ electrolyte

Joonhee Kang [a], Habin Chung [b], Chilhoon Doh [c], Byoungwoo Kang [b, *], Byungchan Han [a, *]

[a] Department of Energy Systems Engineering, DGIST, Daegu, 711-873, Republic of Korea
[b] Department of Materials Science and Engineering, POSTECH, Pohang, 790-784, Republic of Korea
[c] Korea Electrotechnology Research Institute, Changwon, 641-120, Republic of Korea

HIGHLIGHTS

- Calculate diffusion paths and ionic conductivity of a solid-state electrolyte.
- Propose mechanism enhancing Li-ion conductivity by aliovalent element doping.
- Suggest a way to design stable and conductive solid electrolytes.

GRAPHICAL ABSTRACT
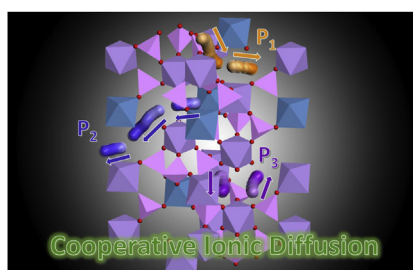
ABSTRACT

Understanding of the fundamental mechanisms causing significant enhancement of Li-ionic conductivity by Al^{3+} doping to a solid LiGe$_2$(PO$_4$)$_3$ (LGP) electrolyte is pursued using first principles density functional theory (DFT) calculations combined with experimental measurements. Our results indicate that partial substitution Al^{3+} for Ge^{4+} in LiGe$_2$(PO$_4$)$_3$ (LGP) with aliovalent (Li$_{1+x}$Al$_x$Ge$_{2-x}$(PO$_4$)$_3$, LAGP) improves the Li-ionic conductivity about four-orders of the magnitude. To unveil the atomic origin we calculate plausible diffusion paths of Li in LGP and LAGP materials using DFT calculations and a nudged elastic band method, and discover that LAGP had additional transport paths for Li with activation barriers as low as only 34% of the LGP. Notably, these new atomic channels manifest subtle electrostatic environments facilitating cooperative motions of at least two Li atoms. Ab-initio molecular dynamics predict Li-ionic conductivity for the LAGP system, which is amazingly agreed experimental measurement on in-house made samples. Consequently, we suggest that the excess amounts of Li caused by the aliovalent Al^{3+} doping to LGP lead to not only enhancing Li concentration but also opening new conducting paths with substantially decreases activation energies and thus high ionic conductivity of LAGP solid-state electrolyte.

© 2015 Elsevier B.V. All rights reserved.

1. Introduction

Lithium ion batteries (LIB) play key roles as power sources in various electronic systems such as portable devices, transportation vehicles and energy storage systems [1–3]. Several urgent issues,

however, need to be solved for a wider-scale of commercialization such as energy density and cyclability. Ensuring system safety over long-term operation of LIB has been particularly challenging satisfying human desire for high power density at the same time. It was well known that the enhancement of energy or power density sometimes led to degradation of structural stability of LIB components. A typical example in this regard is cathode materials with high Ni-compositions, in which improved energy density was accomplished with only increased reactions of the electrodes with liquid-phase organic electrolytes [4,5]. This situation often leads into explosion [6]. Consequently, replacing the liquid-state electrolyte with inert solid-state electrolytes, that is, implementation of all-solid state LIB, has been extensively studied over the last several decades [7–14].

Although many oxides and sulfides were proposed for the candidates of solid-state electrolytes, still substantially lower Li-ionic conductivity hinders the commercialization for any form of the all-solid state LIBs. Recently, Kamaya and associates [9] discovered that the solid state electrolyte $Li_{10}GeP_2S_{12}$ (LGPS) was able to transport Li ions as fast as 1.2×10^{-2} S cm^{-1} at room temperature, which is, in fact, close to the performances of organic liquid electrolytes. However, the LGPS was observed to produce toxic H_2S gas under aqueous media [7,15]. On the other hand, NASICON (Na Super Ionic CONductor)-type materials ($LiM_2(PO_4)_3$, $M = Ti^{4+}$, Ge^{4+}, Hf^{4+}, Sn^{4+} or Zr^{4+}) were known to be not only inert to electrochemical reactions with electrodes [16] but also conductive to Li ions. For example, Aono et al. [17] reported that the Li-ionic conductivity in solid-state $Li_{1.3}Al_{0.3}Ti_{1.7}(PO_4)_3$ electrolyte made from Al^{3+} doping into $LiTi_2(PO_4)_3$ was 7×10^{-4} S cm^{-1} at room temperature without structural degradation. The origin of it was conjectured to the aliovalent dopant Al^{3+} for Ti^{4+}, and for which the Li composition increases to satisfy the overall charge balance. However, Ti in the material was experimentally observed to electrochemically reduce at anode [18,19].

We noted that Ge could completely replace Ti of $Li_{1.3}Al_{0.3}Ti_{1.7}(PO_4)_3$ without structural damage but with slightly lower Li-ionic conductivity [20]. The report also showed that the Li-ionic conductivities in $Li_{1+x}Al_xGe_{2-x}(PO_4)_3$ were substantially sensitive to the doping level (x) of Al, with a maximum at x = 0.5 [16,21]. Many researches to increase conductivity of $Li_{1+x}Al_xGe_{2-x}(PO_4)_3$ were done with various synthetic methods such as solid state reaction, sol–gel, and glass crystallization [16,20,22,23]. However, most of the reports were not extended to obtain detailed mechanistic understandings of increased conductivity. In this paper, we examined two types of solid-state electrolytes, i.e., $LiGe_2(PO_4)_3$ (LGP) and $Li_{1.5}Al_{0.5}Ge_{1.5}(PO_4)_3$ (LAGP), to identify atomic-level structures from a thermodynamic aspect. Further, diffusion paths, activation energies and conductivities of Li in the two model electrolytes were discovered using integrated first principles density functional theory (DFT) calculations and experimental measurements on designed materials.

2. Experimental section

2.1. Computational details

We performed all energy calculations using the Vienna ab-initio simulation package (VASP) [24,25] with projector augmented wave (PAW) [26] pseudo-potentials. The exchange-correlation energy of the electrons was described by employing the generalized gradient approximation (GGA) [27] using the Perdew-Burke-Ernzerhof revised functional for solids (PBEsol) [28]. For structural optimizations, we applied a cutoff energy of 520 eV for the plane wave basis and integrated the first Brillouin zone with the gamma-point scheme with $3 \times 3 \times 1$ k-points. We calculated total energies and

lattice constants with 30% higher cutoff energy and $5 \times 5 \times 1$ k-points but the results only differed 20 meV. To investigate Li-ion diffusion paths in LAGP, we applied ab-initio molecular dynamics (AIMD) simulations in a NVT ensemble under a Nose-Hoover thermostat condition to obtain equilibrated structures [29]. The cutoff energy was 400 eV with $1 \times 1 \times 1$ k-points. The Verlet algorithm, as implemented in VASP, was utilized to track the atomic positions. The time interval of an AIMD simulation was 10 ps (ps) over 5000 steps, each of which was 2 fs (fs). After 50 ps of AIMD simulations, we identified a Li diffusion path, and its activation energy was calculated using the DFT-based nudged elastic band (NEB) method [30]. The NEB is a method to find a minimum energy path for diffusion between initial and final position by assuming imaginary spring forces among all intermediate states of the transport.

2.2. Experimental details

We confirmed the LGP and LAGP structures predicted from the DFT calculations by synthesizing bulk LGP and LAGP electrolytes through a solid-state reaction process described in our previous paper [31]. Li_2CO_3, Al_2O_3, GeO_2, and $(NH_4)_2HPO_4$ were used as the precursors for LAGP and also for LGP except Al_2O_3. The synthesized LAGP and LGP contained impurities such as $AlPO_4$, GeO_2 and $Li_4P_2O_7$ but less than total 1.5wt%. X-ray diffraction (XRD) patterns were obtained for a pellet-shaped LAGP material using a Rigaku XRD (D/MAX-2500/PC) with Cu Kα radiation in the 2θ range from 10° to 60° at a rate of 2° min, and they were further analyzed using MDI jade 6 [31]. Electrochemical impedance spectroscopy (EIS, Ivium) [31] was measured to obtain bulk ionic conductivity and activation energy of samples. The prepared pellets which were pressed by 540 MPa and sintered at 800 °C for 2 h in box furnace were disk-shaped with diameter of 1.2 cm and thickness of 0.16 cm. Ag paste was applied to both sides of the pellet for ionic blocking electrodes and dried at 200 °C for 10 min. The impedance spectroscopy of the samples was measured over the range of frequencies from 1 MHz to 0.01 Hz with an applied voltage of 0.1 V. The data were described as customized equivalent circuits using ZView2 impedance software. The conductivity of bulk and grain boundary can be distinguished at low temperatures. Therefore, the impedance spectra were measured at temperatures from RT to −40 °C to obtain Arrhenius plots for bulk. During measurements, the sample was held in a temperature and humidity test chamber (Jeio tech., Republic of Korea) to maintain and control the temperature and humidity.

3. Results and discussion

3.1. Model systems

Our model systems for LGP and LAGP (each 6 formula unit) are illustrated in Fig. 1. LGP and LAGP are rhombohedral crystal structures (space group, $R\bar{3}c$) with the MO_6 (M = Ge, Al) and PO_4 moieties serving as octahedrons and tetrahedrons, respectively. Every two octahedrons share corners with three nearby tetrahedrons. For the LAGP model, we replaced three of twelve Ge with Al to render the doping level $x = 0.5$ in the formula unit $Li_{1+x}Al_xGe_{2-x}(PO_4)_3$; thus, there are three additional Li ions relative to LGP (i.e., there are six Li in LGP and nine in LAGP in our model systems.). To identify energetically stable site for Al^{3+}, we evaluated total energies of the LAGP materials with all possible Al configurations. Our results indicated that the doped Al^{3+} form a configuration with each 8.43 Å away from the nearest neighbors.

Extensively utilizing DFT calculations we searched for thermodynamically stable arrangements of Li in the LGP and LAGP
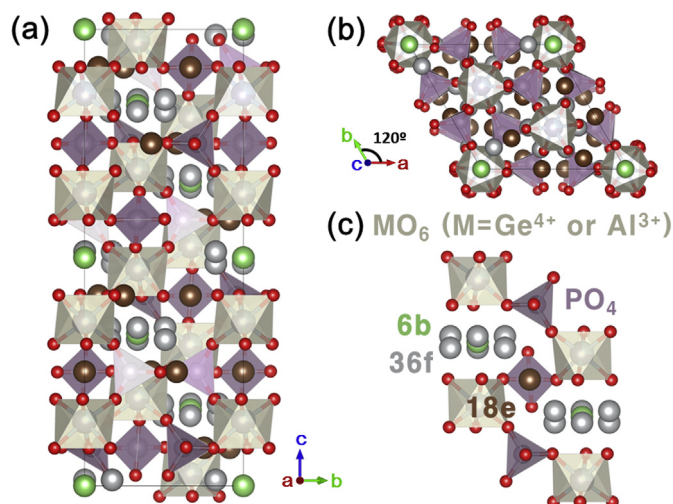
Fig. 1. LGP and LAGP possess the same rhombohedral structure ($R\bar{3}c$) viewed along the a-axis in (a) and along the c-axis in (b). Ivory-colored octahedrons denote GeO_6 or AlO_6 and tetrahedrons of PO_4 are represented in violet color. Three different sites for Li, 6b (green), 18e (brown) and 36f (silver) are shown in (c). (For interpretation of the references to colour in this figure legend, the reader is referred to the web version of this article.)

materials. Initially, Li were allocated arbitrarily at three different kinds of Wyckoff sites [32]: 6b, 18e and 36f. The 6b site is surrounded by six O atoms, which is in turn bordered by six 36f sites located 1.65 Å away. The 18e position is at the middle of the two different 6b sites. Our DFT calculations clearly showed that all of the six Li in the LGP material preferentially occupy the 6b sites only. For the LAGP, we assigned four pairs of Li at the sites of (6b, 18e), (6b, 36f), (18e, 36f) and (36f, 36f) and the rest Li at the 6b site. We disregarded any arrangement with three Li because of too short interatomic distances to make the material.

Previous report [33] suggested that Li in NASICON-type structure should be at 6b site and any excess Li caused by aliovalent doping reside at 18e sites. Our DFT calculations, however, clearly showed that a pair of Li in the LAGP thermodynamically prefers the two 36f sites instead of one 6b and one 18e site, as denoted in Fig. 2. The mutual distance between the two sites is approximately 3.29 Å, which is much longer than 2.98 Å of a bulk bcc Li crystal. Our DFT
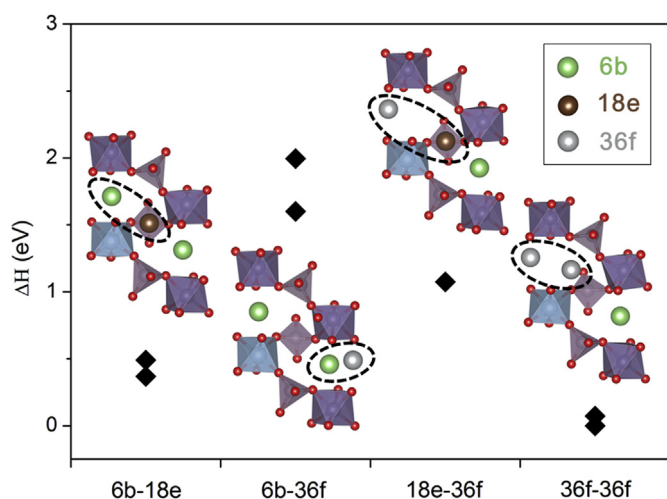
calculations on Li positions in the LAGP show that three Li at 6b sites, and six at 36f. Interestingly, one Li pair always occupies 36f sites nearby.

As depicted in Fig. 3, our experimental XRD patterns also clearly showed that the LAGP material possesses rhombohedral symmetry ($R\bar{3}c$), which well agrees with the DFT calculations. The slight deviations at the peak positions near the high angle regions were caused by slight lattice mismatches between the experimental samples and the computational model systems, as indicated in Table 1. The lattice constant obtained by DFT calculation with GGA method overestimated experimentally measured one by less than 1%, which is well known [34].

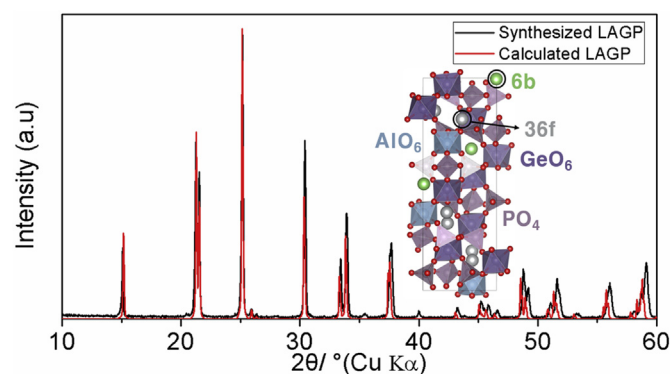### 3.2. Ab-initio molecular dynamic simulations

Using AIMD simulations we identified atomic-scale Li diffusion mechanisms in the LGP and LAGP models. The initial configurations were the same as described in section 3.1 (six Li at all 6b sites in the LGP while three Li at 6b sites and six Li at 36f sites in the LAGP). We thermally equilibrated LGP (LAGP) at temperatures of 1073 K (873 K) as a previous report [29] proposed that the thermal conditions should not change outcomes at room temperature.

Fig. 4 illustrates the trajectory of Li motions captured every 0.1 ps during AIMD simulations for 50 ps. It indicates that Li at the sites of 6b and 36f in LAGP gradually move into other 6b and 36f nearby the original positions via 18e (brown) (in web version). On the contrary, Li in the LGP model show completely different behaviors. As illustrated at Fig. 4(a) Li is not able to diffuse into the other 36f through 18e sites, even at higher temperatures than LAGP. These results imply that Li should diffuse much faster in LAGP than in LGP being in consistent with our Li ion conductivity experiments ($\sigma_{LGP} = 1.23 \times 10^{-8}$ S cm^{-1}, $\sigma_{LAGP} = 3.02 \times 10^{-4}$ S cm^{-1}, described at '3.4. Ionic conductivity' section).

While our AIMD simulations clearly identified the diffusion paths of Li in the two model systems, overall calculation time was too costly to obtain Li diffusion coefficients. Thus, we utilized the NEB method.

3.3. NEB simulations

To understand how the distinctive diffusion behaviors affect Li-ionic conductivities in the two model systems we employed the DFT-based NEB method [35,36] and evaluated activation energies along plausible transport paths of Li. As stated at section 3.2 we identified three different routes for Li diffusion by AIMD

Fig. 2. DFT calculated energies for different configurations of four pairs of Li in LAGP at the sites (6b, 18e), (6b, 36f), (18e, 36f) and (36f, 36f).


Fig. 3. XRD patterns of synthesized LAGP (black color) and calculated LAGP (red color) structures. The inserted picture is the model system of LAGP, which has three Li atoms at 6b sites (green) and six Li atoms at 36f sites (silver). (For interpretation of the references to colour in this figure legend, the reader is referred to the web version of this article.)

	a (Å)	b (Å)	c (Å)	V (Å^3)
$Li_{1.0}Ge_{2.0}(PO_4)_3$ (Expt.)	8.2683	8.2683	20.4920	1213.25
$Li_{1.0}Ge_{2.0}(PO_4)_3$ (Calc.)	8.3560	8.3562	20.5389	1242.01
$Li_{1.5}Al_{0.5}Ge_{1.5}(PO_4)_3$ (Expt.)	8.2648	8.2648	20.6276	1220.25
$Li_{1.5}Al_{0.5}Ge_{1.5}(PO_4)_3$ (Calc.)	8.3427	8.3289	20.7878	1248.98
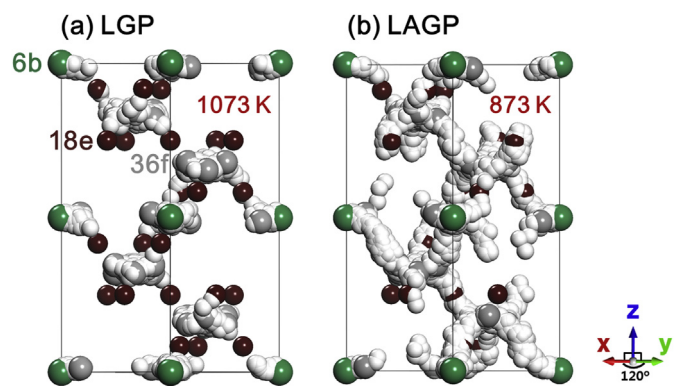
Fig. 4. Transport trajectories of Li simulated using AIMD over 50 ps in LGP at 1073 K (a) and LAGP at 873 K (b).

simulations: we classified them with paths of P_1, P_2 and P_3 as illustrated at Fig. 5.

Along P_1 one of two Li at 6b moves to 36f, the other Li begins to diffuse into other 36f just when the first Li passes through 18e (the distance between 18e and 6b is about 3.04 Å, which is almost identical to that of bulk bcc Li). As the result, the two 6b sites, which were initially occupied by two Li, become empty. The origin of this cooperative movement of the two Li ions is caused by strong repulsive electrostatic force at short mutual distance. It is noteworthy that this process is very different from what may be expected, i.e., a stepwise diffusion of a single Li ion at each stage. Our results imply that diffusion of Li along the P_1 path occurs by cooperative interactions of at least two Li ions triggered by strong electrostatic forces.
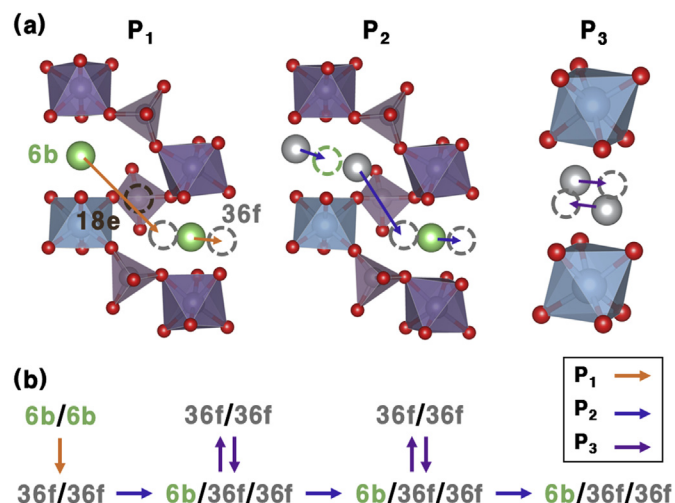

Fig. 5. Three types of diffusion paths of Li in the LGP and LAGP model systems, as established in our AIMD simulations. Solid spheres indicate the initial configurations, whereas dash-lined circles represent the final configurations. The specific sites and directions of each diffusion process are indicated by arrows in (b).

The P_2 path is available to Li in the LGP model once the diffusion process along the P_1 route is completed. We note that the P_2 path is always available in the LAGP, where three Li ions initially located at the 6b (one Li) and 36f (two Li) sites transport into other 6b and 36f sites; consequently, the configuration after the diffusion is identical to the initial configuration, as depicted in Fig. 5(a).

The diffusion process along P_3 shown in Fig. 5(b) simply affords the mutual exchange of two Li ions, leading to no net movement. The P_3 route may be important when other diffusion paths (i.e., P_1 or P_2) are blocked by impurities or defects since it allows changing the direction of Li motion.

Using the DFT-based NEB method we evaluated activation energies along the diffusion paths P_1, P_2 and P_3. Fig. 6 indicates that Li in the LGP and LAGP models experiences significantly different activation energies: 0.787 (LGP) and 0.673 eV (LAGP). This can be rationalized in terms of the channel sizes for Li diffusion processes. The ionic size of the Al^{3+} dopant ($r = 0.535$ Å) is slightly larger than Ge^{4+} ($r = 0.530$ Å) causing the lattice parameter in the c-axis of LAGP to be elongated as well observed by experiment [37]. Additionally, the bond distances between Li at 6b and its nearest neighbor O in the LGP and the LAGP were calculated as 2.196 and 2.243 Å, respectively. Consequently, the diffusion channels for Li are larger in the LAGP than the LGP material, leading to faster transport of Li. Activation barriers along the P_1 in both the LGP and LAGP are
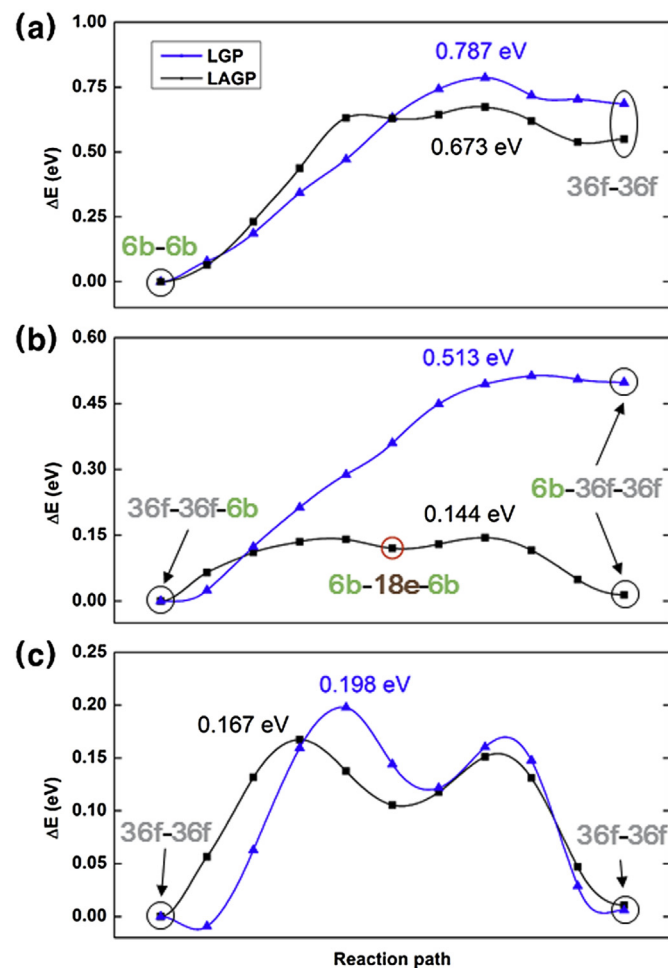
Fig. 6. DFT-based NEB calculated activation energies of a Li ion diffusing along P_1 (a), P_2 (b) and P_3 (c). Blue lines indicate LGP and black lines indicate LAGP. (For interpretation of the references to colour in this figure legend, the reader is referred to the web version of this article.)

much higher than the P_2 and P_3. This is due to structural instability by the diffusion through P_1. Our DFT calculations indicated that structures with both 6b and nearby 36f empty, which is the atomic configuration after the diffusion along the P_1, is thermodynamically unstable as much as 0.686 eV (0.499 eV) with respect to the initial arrangement of Li in the LGP (LAGP) models.

In contrast, activation energy of Li diffusion along the P_2 is significantly lower than through the P_1. Clearly, this implies that the channel size is not the only factor to describe the behavior; instead, a completely new driving force may underlie. We propose that the governing mechanism is in the repulsive electrostatic force among the Li along the P_2, which is much stronger than along the P_1. As described the previous section, diffusion of Li along P_1 should occur in the LGP before the P_2 route is utilized, but this is thermodynamically not plausible. This is why the activation energy along P_2 in the LGP model does not decrease as much as in the LAGP model. In contrast, the high Li concentration in the LAGP model caused by the aliovalent doping of Al^{3+} provide an opportunity for Li to exploit the P_2 directly without requiring the P_1 route.

Fig. 6(b) shows that the 18e site (marked by a reddish open circle) is a metastable site along the diffusion pathway along the P_2 channel. Accordingly, Li approaching to the site may prefer to occupy nearby empty 36f sites from a thermodynamic aspect.

Activation energies of Li along the P_3 path were calculated to be 0.198 and 0.167 eV in the LGP and LAGP materials, respectively. We postulated that the identical diffusion mechanism suggested for P_1 (i.e., the size of the diffusion channel) is operative in the P_3 as well.

3.4. Li-ionic conductivity

Based on our calculations and the Arrhenius law [38], we evaluated Li-ionic conductivity as a function of temperature, σ_T, as shown in Eq. (1):

$$\sigma_T = \frac{(ze)^2 C_{Li} l^2 \nu_0}{6kT} \exp\left(\frac{-E_a}{kT}\right) \qquad (1)$$

where e, C_{Li} and l indicate the electronic charge of an electron (1.6×10^{-19} C), the Li ion concentration and the hopping distance between two stable diffusion sites, respectively. ν_o is the attempting frequency of the Li ion, E_a denotes the activation energy for diffusion and k is Boltzmann's constant. In our LAGP model system, C_{Li} and l are 7.206×10^{21} atoms cm^{-3} and 6.25 Å, respectively. We used a typical value of 10^{13} Hz for ν_o [39]. To calculate Li conductivity we had to know relative contribution from P_1 and P_2 paths, which is determined by fractional availability of the two paths by Li. We assumed 40% of total Li-ions transport along P_1 and the rest through P_2. With this hypothesis, which should be validated by future work, we predicted the Li ion conductivity in Bulk by Arrhenius equation to compare the experimental measurements. Even though, there is this single approximation in our calculations the outcomes fairly well agreed experimental results over entire range of temperatures considered in this paper.

Fig. 7 shows Nyquist plots of LAGP measured at various temperatures from room temperature to $-40\,°C$. At room temperature, the frequency range of Li ion conduction in bulk is over 1 MHz so only semicircle of grain boundary and tail of electrode polarization appear. As the temperature decrease, the resistances increase and the frequencies for the bulk conduction decrease and then bulk semicircle appears below 0 °C. The intersection of fitted two semicircles with x-axis means bulk resistance. LGP has four orders lower conductivity than LAGP at room temperature and the impedance data of LGP below $-10\,°C$ could not obtained because the resistances were too high.
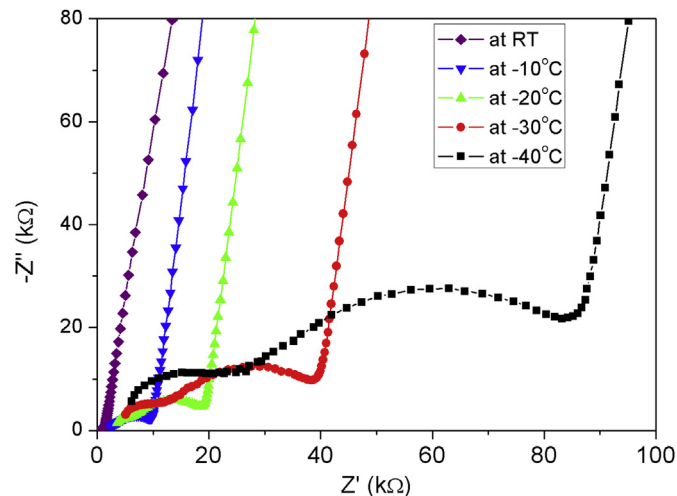

Fig. 7. Li-ionic Nyquist plots of LAGP from EIS at various temperatures, from RT to $-40\,°C$.

We plot Li-ionic conductivities of LAGP as a function of temperature in Fig. 8. At $T = 298$ K, the calculated Li conductivity in the LGP and LAGP models are predicted to be 5.79×10^{-9} S cm^{-1} and 2.83×10^{-4} S cm^{-1}. The experimental Li-ionic conductivity in LAGP was measured as 3.02×10^{-4} S cm^{-1} at room temperature with 0.37 eV of its activation energy. At the same condition, LGP showed almost 4 orders lower value, 1.23×10^{-8} S cm^{-1} than LAGP. The experimental measurements confirmed the results from our calculations at 298 K, within an error of 5%. The slight differences in calculated and experimentally measured conductivities may be originated from impurities in the solid-state electrolyte samples [40]. Over the last two years we experimented more than ten LAGP samples to measure Li-ionic conductivity for various research works. The errors of the conductivity was about 10% ($1.2-1.4 \times 10^{-4}$ S cm^{-1}) at room temperature. We omitted the error bar in our manuscript since the Arrhenius plots (EIS at various temperature) were not obtained from every samples.

In summary, using integrated first principles DFT calculations, AIMD simulations and experimental measurements, we studied the underlying mechanisms of Li ion conductivities in a solid-state $LiGe_2(PO_4)_3$ material by Al^{3+} dopant. Our results indicated that
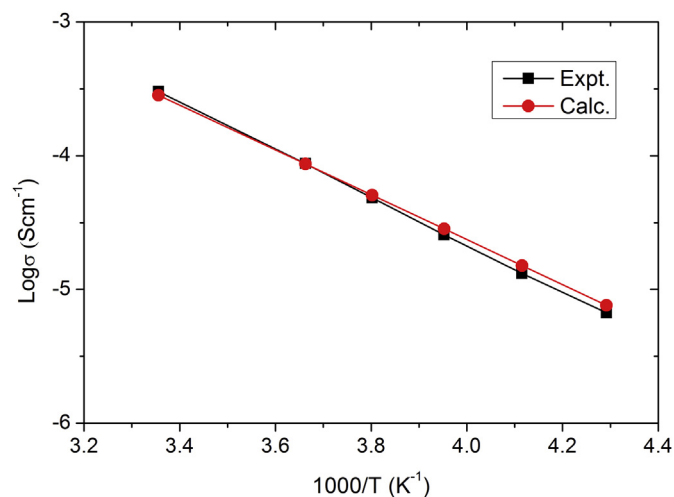

Fig. 8. Li-ionic conductivities as a function of temperature for the LAGP electrolyte, as predicted using DFT calculations and measured experimentally.

the aliovalent Al^{3+} doping for Ge^{4+} provides three key benefits for Li transport: higher Li ion carrier concentration, a bigger diffusion channels and new diffusion paths with much lower activation barriers. Under such circumstances, at least two Li ions could move cooperatively leading to much better ionic conductor.

Based on our results we suggest a way to improve stability and Li-ionic conductivity of a solid-state electrolyte. Key control factor is to identify aliovalent doping elements enabling to create new diffusion paths for Li with less activation barriers. In the process it is very useful to utilize first principles-based computational screening due to its high throughput power in sorting out proper candidates of the doping elements [41] and in estimation of thermodynamic stability and Li-ionic conductivity after doping to the electrolyte. Of course, rigorous validation for the prediction by experiments should support the approach.

4. Conclusion

The mechanism for increased ionic conductivity from LGP to LAGP was understood by first principles DFT calculations with experimental measurements. Opposite to common knowledge, when two Li ions are located in two 6b sites, excess Li induced by Al^{3+} doping for Ge atoms thermodynamically prefer 36f positions rather than 18e sites. Li-ionic conductivity was enhanced as high as four orders of magnitude in LAGP compared to LGP. It was originated not just from increased Li concentration but by newly created diffusion paths (P_2) with substantially reduced activation energies. Cooperative motions of at least two Li was proposed as underlying mechanism for the activation barrier change. Our approach, which can identify thermodynamic stability of doped electrolyte materials and kinetic transport of ions through them, can be easily applied to screen promising solid-state electrolytes with not only high ionic conductive paths (such as P_2 path in this paper) but also thermodynamic durability, and consequently will be useful for guiding rational design of all-solid state LIB systems.

Conflict of interest

The authors declare no competing financial interests.

References

[1] M. Armand, J.-M. Tarascon, Nature 451 (2008) 652–657.
[2] P. Simon, Y. Gogotsi, Nat. Mater. 7 (2008) 845–854.
[3] B. Kang, G. Ceder, Nature 458 (2009) 190–193.
[4] Y.-K. Sun, S.-T. Myung, B.-C. Park, J. Prakash, I. Belharouak, K. Amine, Nat. Mater. 8 (2009) 320–324.
[5] T. Ohzuku, Y. Makimura, Chem. Lett. (2001) 744–745.
[6] H. Xiang, H. Wang, C. Chen, X. Ge, S. Guo, J. Sun, W. Hu, J. Power Sources 191 (2009) 575–581.
[7] G.y. Adachi, N. Imanaka, H. Aono, Adv. Mater. 8 (1996) 127–135.
[8] R. Murugan, V. Thangadurai, W. Weppner, Angew. Chem. Int. Ed. 46 (2007) 7778–7781.
[9] N. Kamaya, K. Homma, Y. Yamakawa, M. Hirayama, R. Kanno, M. Yonemura, T. Kamiyama, Y. Kato, S. Hama, K. Kawamoto, Nat. Mater. 10 (2011) 682–686.
[10] K. Chen, Y. Shen, J. Jiang, Y. Zhang, Y. Lin, C.-W. Nan, J. Mater. Chem. A 2 (2014) 13332–13337.
[11] D. Safanama, D. Damiano, R.P. Rao, S. Adams, Solid State Ionics 262 (2014) 211–215.
[12] M. Kotobuki, M. Koishi, Y. Kato, Ionics 19 (2013) 1945–1948.
[13] V. Thangadurai, S. Narayanan, D. Pinzaru, Chem. Soc. Rev. 43 (2014) 4714–4727.
[14] S. Kumazaki, Y. Iriyama, K.-H. Kim, R. Murugan, K. Tanabe, K. Yamamoto, T. Hirayama, Z. Ogumi, Electrochem. Commun. 13 (2011) 509–512.
[15] L.J. Miara, S.P. Ong, Y. Mo, W.D. Richards, Y. Park, J.-M. Lee, H.S. Lee, G. Ceder, Chem. Mater. 25 (2013) 3048–3055.
[16] X. Xu, Z. Wen, X. Wu, X. Yang, Z. Gu, J. Am. Ceram. Soc. 90 (2007) 2802–2806.
[17] H. Aono, E. Sugimoto, Y. Sadaoka, N. Imanaka, G.y. Adachi, J. Electrochem. Soc. 137 (1990) 1023–1027.
[18] P. Birke, F. Salam, S. Döring, W. Weppner, Solid State Ionics 118 (1999) 149–157.
[19] P. Maldonado-Manso, E.R. Losilla, M. Martínez-Lara, M.A. Aranda, S. Bruque, F.E. Mouahid, M. Zahir, Chem. Mater. 15 (2003) 1879–1885.
[20] J. Fu, Solid State Ionics 104 (1997) 191–194.
[21] M. Cretin, P. Fabry, J. Eur. Ceram. Soc. 19 (1999) 2931–2940.
[22] M. Zhang, K. Takahashi, N. Imanishi, Y. Takeda, O. Yamamoto, B. Chi, J. Pu, J. Li, J. Electrochem. Soc. 159 (2012) A1114–A1119.
[23] J.S. Thokchom, N. Gupta, B. Kumar, J. Electrochem. Soc. 155 (2008) A915–A920.
[24] G. Kresse, J. Hafner, Phys. Rev. B 47 (1993) 558.
[25] G. Kresse, J. Furthmüller, Phys. Rev. B 54 (1996) 11169.
[26] P.E. Blöchl, Phys. Rev. B 50 (1994) 17953.
[27] J.P. Perdew, K. Burke, M. Ernzerhof, Phys. Rev. Lett. 77 (1996) 3865.
[28] J.P. Perdew, A. Ruzsinszky, G.I. Csonka, O.A. Vydrov, G.E. Scuseria, L.A. Constantin, Z. Xiaolan, K. Burke, Phys. Rev. Lett. 100 (2008).
[29] S.P. Ong, Y. Mo, W.D. Richards, L. Miara, H.S. Lee, G. Ceder, Energy & Environ. Sci. 6 (2013) 148–156.
[30] G. Henkelman, H. Jonsson, J. Chem. Phys. 113 (2000) 9978–9985.
[31] H. Chung, B. Kang, Solid State Ionics 263 (2014) 125–130.
[32] S. Roy, P.P. Kumar, J. Mater. Sci. 47 (2012) 4946–4954.
[33] A. Martínez-Juárez, C. Pecharromán, J.E. Iglesias, J.M. Rojo, J. Phys. Chem. B 102 (1998) 372–375.
[34] J. Hafner, J. Comput. Chem. 29 (2008) 2044–2078.
[35] Z. Wang, R. Peng, W. Zhang, X. Wu, C. Xia, Y. Lu, J. Mater. Chem. A 1 (2013) 12932–12940.
[36] Z. Wang, Q. Su, H. Deng, W. He, J. Lin, Y.Q. Fu, J. Mater. Chem. A 2 (2014) 13976–13982.
[37] R.t. Shannon, Acta Crystallogr. Sect. A: Cryst. Phys. Diffr. Theor. General Crystallogr. 32 (1976) 751–767.
[38] P.G. Bruce, Solid State Electrochemistry, Cambridge University Press, 1997.
[39] J. Narváez-Semanate, A. Rodrigues, Solid State Ionics 181 (2010) 1197–1204.
[40] N. Kosova, E. Devyatkina, A. Stepanov, A. Buzlukov, Ionics 14 (2008) 303–311.
[41] S.H. Noh, M.H. Seo, J.K. Seo, P. Fischer, B. Han, Nanoscale 5 (2013) 8625–8633.